DE GRUYTER

Z. Phys. Chem. 2016; 230(3): 313–338

Shinya Hosokawa*, Jens Rüdiger Stellhorn,
Wolf-Christian Pilgrim, and Jean-François Bérar

Anomalous X-ray Scattering on Semiconducting Glasses at ESRF: Review in Recent Fifteen Years

Abstract: The most difficult issue for the structural characterizations for non-crystalline multi-component materials is to determine partial structures because $n(n+1)/2$ scattering experiments with different scattering cross-sections are necessary for n-component materials. More than three decades have already passed through since anomalous X-ray scattering (AXS) using synchrotron radiation (SR) was expected as a promising tool for investigating partial structures. Compared with a related method, X-ray absorption fine structure, however, AXS is still rarely used owing to difficulties in the experiments and data analyses. We have developed a new detecting system, which can fully utilize intense X-ray fluxes from third-generation SR facilities. Using this detecting system, we have carried out many AXS experiments at the beamline BM02 of the ESRF on several semiconducting glasses. The obtained differential structure factors were analyzed using reverse Monte Carlo modeling to draw three-dimensional atomic configurations. In this article, we review results of semiconducting glasses, and describe the structure-property relations in these glasses.

Keywords: Atomic Structure, Non-Crystalline Materials, Partial Structure, Synchrotron Radiation, Chalcogenide Glasses.

*Corresponding author: Shinya Hosokawa, Department of Physics, Graduate School of Science and Technology, Kumamoto University, 2-39-1 Kurokami, Chuo-ku, Kumamoto, 860-8555, Japan; and Department of Chemistry, Physical Chemistry, Philipps University of Marburg, Hans-Meerwein-Str., Marburg, 35032, Germany, e-mail: hosokawa@sci.kumamoto-u.ac.jp
Jens Rüdiger Stellhorn, Wolf-Christian Pilgrim: Department of Chemistry, Physical Chemistry, Philipps University of Marburg, Hans-Meerwein-Str., Marburg, 35032, Germany
Jean-François Bérar: Institut Néel, CNRS/Université Joseph Fourier, 25 rue des Martyrs, BP 166, Grenoble cedex 9, 38042, France

1 Introduction

X-ray diffraction (XRD) is usually applied for investigating the structures of crystalline materials. The XRD spectra are mainly composed of Bragg peaks generated by coherently and elastically scattered X-rays from the atomic arrays in crystals. Other contributions in the experimental XRD spectra are Compton scattering and fluorescent X-rays. These appear as backgrounds between the Bragg peaks, and the intensities are much smaller. Thus, these non-elastic contributions can be easily subtracted. Even a material is composed of many elements and the atomic coordinates are very complicated, such as protein crystals with more than 10 000 atoms in the unit cell, the atomic configurations can nowadays be determined using intense synchrotron radiation (SR) sources and Rietveld analysis [1].

For non-crystalline materials, scattering spectra show only weak hallow patterns [2]. Although in principle the structural information can be evaluated, there are some serious problems that cannot easily be solved:

1. The above mentioned non-elastic contributions are highly mixed with the elastic signal, and should be removed using a detector with a good energy resolution.

2. Even if the elastic signals are successfully extracted, they are the mixtures of the partial structure factors, $S_{ij}(Q)$, of the constituent elements. For n-component alloys, the number of the partials reaches $n(n+1)/2$, e.g., binary gives three partials, ternary six, and quaternary ten, as quoted in Waseda's textbooks [2–4] and review articles [5–7].

The total structure factor, $S(Q)$, is expressed as

$$S(Q) = \sum_{i=1}^{N} \sum_{j=1}^{N} W_{ij}(Q) S_{ij}(Q). \tag{1}$$

Here, the weighting factors, W_{ij}, can be obtained as

$$W_{ij}(Q) = x_i x_j f_i f_j / \langle f \rangle^2, \tag{2}$$

where x_i and f_i are the concentration and atomic form factor of i-th element, respectively. Thus, several diffraction data with different scattering processes, i.e., different f_i values, are necessary to obtain $S_{ij}(Q)$s. Neutron diffraction (ND) is helpful, in particular, when using isotope-enriched samples, which give largely different W_{ij}s [6]. Since the properties of glasses often depend on the thermal history, and the isotopes are very costly, however, an alternative method is highly desired to obtain $S_{ij}(Q)$s.

Anomalous X-ray scattering (AXS) [2–4], or resonant elastic X-ray scattering utilizes an anomalous variation of f near an absorption edge of an element. The complex f is given as

$$f(Q, E) = f_0(Q) + f'(E) + if''(E), \qquad (3)$$

where f_0 is the usual energy-independent main term, and f' and f'' are the real and imaginary parts of the anomalous term, respectively. When the incident X-ray energy approaches an absorption edge k of a constituent element, the energy-dependent f' and f'' become important, resulting in a decrease in scattering intensity. The contrast between the scattering intensities close to an absorption edge and a 'normal' scan, highly enhances the partial contributions concerning the element, and suppresses the other partials.

The AXS technique was firstly adopted using X-ray tubes with some different target materials to study partial atomic structures in non-crystalline GeO_2 in 1974 by Bondot [8]. Several metallic liquid and amorphous alloys were investigated with the same technique by Waseda and Tamaki [9, 10]. A significant improvement of the AXS data was achieved by using SR as the X-ray source on amorphous chalcogenide semiconductors, GeSe and $GeSe_2$ [11], and "AXS using SR" was viewed as a promising tool.

Since then, more than three decades have passed. Compared to a related method for structural analysis, X-ray absorption fine structure (XAFS), however, AXS is still rarely used although in contrast to XAFS, it also provides information on the intermediate-range order (IRO). The cautious progress of this method is related to the difficulties in correcting the raw data for fluorescence and Compton contributions, which are complicated and time-consuming procedures. Although recent developments in third-generation SR sources led to a tremendous increase of incoming flux, this did not help to solve the problems of the above mentioned parasitic scattering contributions, and these problems still remain as a challenging task. Also, the experimental determination of the anomalous terms is very difficult.

We have developed a detecting system effective for intense third-generation SR [7, 12–15]. In this paper, we report in detail the feasibility of this system by comparing with the previous systems employed widely, and the most typical AXS results on prepeaks or first sharp diffraction peaks (FSDP) in Ge–Se [16, 17] and As–Se [18, 19] chalcogenide glasses, Ag–GeSe room-temperature superionic conducting glass [20, 21], and $Ge_2Sb_2Te_5$ digital versatile disk (DVD) material [22]. We have introduced this technique in several papers [7, 12, 13, 16]. However, it is worth reviewing once more with a special regard to the procedure of the development for the future plan of well-established AXS experiments.

2 Limitations of previous anomalous X-ray scattering

The principle of AXS is widely known and given in literatures [3, 7, 16, 23]. The intensity contrast, $\Delta_k I$, between two scattering functions can be obtained for the k absorption edge of an element if they are measured closely below the absorption edge (E_{near}, typically some 10 eV) and further below the edge (E_{far}, typically some 100 eV). This contrast can then be expressed as

$$\Delta_k I(Q, E_{\text{far}}, E_{\text{near}}) \propto \Delta_k[\langle f^2 \rangle - \langle f \rangle^2] + \Delta_k[\langle f \rangle^2]\Delta_k S(Q). \tag{4}$$

Here, $\Delta_k[\ ]$ indicates the difference of values in the bracket at the energies of E_{far} and E_{near}, close to the absorption edge k of the element, and $\langle\ \rangle$ represents the chemical average. The differential structure factor, $\Delta_k S(Q)$, in Equation 4 can again be expressed by a linear combination of $S_{ij}(Q)$s as

$$\Delta_k S(Q) = \sum_{i=1}^{N} \sum_{j=1}^{N} W_{ij}(Q, E_{\text{far}}, E_{\text{near}}) S_{ij}(Q), \tag{5}$$

with different W_{ij}s given by

$$W_{ij}(Q, E_{\text{far}}, E_{\text{near}}) = x_i x_j \frac{\Delta_k[f_i f_j]}{\Delta_k[\langle f \rangle^2]}. \tag{6}$$

It should be noted that compared to $S(Q)$, $\Delta_k S(Q)$ highly enhances the partial contributions from the element with k edge, and suppresses the other partials.

From the above principle of AXS, the difficulty of this technique seems to lie only on the precise determination of the f function, which is well-known to be highly dependent on the chemical environments or electronic conditions such as the valence number and chemical bonds.

The optical theorem [24] directly relates f'' to the atomic absorption coefficient for an atom, μ_{a}, as

$$f'' = \frac{m_e c \varepsilon_0 E}{e\hbar} \mu_{\text{a}}, \tag{7}$$

where E is the X-ray energy and others have their usual meanings. The f' term is related to the f'' part by a Kramers–Kronig transformation expressed as

$$f'(E) = \frac{2}{\pi} \int_0^\infty \frac{E' f''(E')}{E^2 - E'^2} dE'. \tag{8}$$
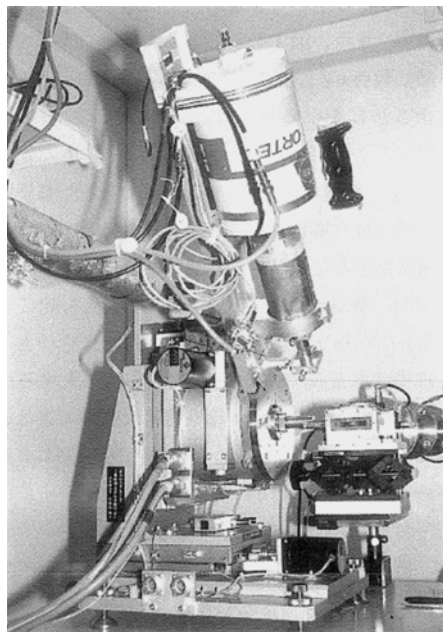
Figure 1: AXS goniometer with a SSD detector installed at PF-KEK. After [29].

Thus, it is necessary to measure X-ray absorption spectra in a wide X-ray energy range and precisely near the absorption edge to obtain reliable values for f' and f''.

Theoretical values [25, 26] are usually used for the analyses of AXS data. However, discrepancies of f' values are frequently reported near absorption edges [4, 6, 27]. For example, the theoretical f' value of Ge in GeSe$_2$ glass at 15 eV below the K edge is about 14% smaller than a corrected value [17] obtained by a comparison with a result of the neutron diffraction using isotope-enriched samples [28]. This problem can be perfectly solved by an attentive absorption measurement and a subsequent careful data analysis.

However, the real thorny path was not such a straightforward subject. The crucial problem was that no suitable detector can be prepared for the scattered X-rays for intense third-generation SR facility. Figure 1 shows a photograph of an AXS goniometer [29] installed at PF-KEK, which is a typical second-generation synchrotron source. There, a pure Ge solid-state-detector (SSD) is mounted on the goniometer. This type of X-ray detector is very sensitive, and can collect energy-resolved data of scattered X-rays. Thus, it is very suitable for the second-generation SR sources. When this detector is used for intense third-generation SR facilities, however, two essential problems were revealed; a moderate (not enough) energy resolution and a long dead time.
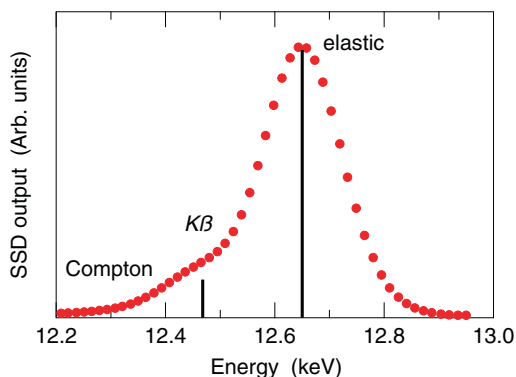
Figure 2: Typical SSD signal as a function of X-ray energy with the energy resolution of ∼ 200 eV FWHM. The spectrum was estimated for GeSe$_2$ glass at the incident energy of 20 eV below the Se K absorption edge at the scattering angle of about 45°.

Figure 2 shows a typical SSD output as a function of X-ray energy. The spectrum was estimated for GeSe$_2$ glass at the incident energy of 20 eV below the Se K absorption edge (12.658 keV) at the scattering angle of about 45°. Incident X-ray energies were calibrated using the absorption edge of each constituent element of the samples. The energy resolution is about 200 eV full-width at half-maximum (FWHM). The long bar shows the elastic energy, and the shoulder on the low energy side of the elastic peak indicates the Se $K\beta$ fluorescent X-rays given by the short bar. The Compton scattering contribution is located beneath these contributions in a wide energy range. As seen in the figure, it is not easy to evaluate the elastic intensity from such a complex spectrum.

A usual way to evaluate the pure elastic signal was that using single channel analyzers, the total counts of the spectra including non-elastic contributions and $K\alpha$ signals in the lower energy regions were simultaneously measured, and the $K\beta$ contributions were subtracted by assuming that the ratio of the $K\beta$ and $K\alpha$ signals was unchanged [3, 4]. Also, the Compton scattering contribution becomes negligible by taking a contrast between the two scattering spectra at E_{far} and E_{near}.

However, there is no guarantee that the $K\beta/K\alpha$ intensity ratio is always the same to make such an estimate. Even if the assumption is correct or the error is extremely small, such a calculation takes a long time, and it is difficult to complete it during the limited beamtime for AXS experiments. For example, our AXS analysis on glassy As$_2$Se$_3$ [30] took three weeks until we obtained $\Delta_k S(Q)$ near the As and Se K absorption edges.

The most serious problem of the SSD detector is, however, not so trivial and is related to the long blind time of the SSD detector. Typical SSD detectors have a blind time of about 1 μs, and the linear response of the detector is lost over a count rate of 20 000 cps [31]. Note that this value is not elastic scattering only, but the total number of incoming X-rays including several fluorescent and Comp-

ton scattering X-rays. Typically, the fraction of elastic scattering is only 10% (see Figure 4 of Reference [31]), and thus, the maximum rate for the elastic signal is only 2000 cps. Since AXS typically needs 1 000 000 counts at the $S(Q)$ maximum, 500 Q points, and 2 scans for each absorption edge, 500 000 s ~ 140 h ~ 6 d are necessary to obtain only one $\Delta_k S(Q)$. If the blind time corrections are made, more scattering intensity (up to 200 000 cps [31]) can, in principle, be measured and a reduction of the experiment duration down to ~ 14 h per $\Delta_k S(Q)$ is possible, although the error should be carefully taken into account in the data reduction. Although such corrections are possible, intense third-generation SR cannot help to improve the statistical quality of the $\Delta_k S(Q)$ data when using a SSD detector.

3 Present detecting system at BM02/ESRF

To overcome the above-mentioned difficulties of the detecting system, in particular, the counting rate and energy resolution, we recall a usual NaI scintillation counter having a blind time of typically ~ 10 ns. However, the scintillation counter has mostly no energy resolved function, and thus, an energy analyzer is necessary to discriminate the elastic signal from other contributions.

Tests of some different energy analyzer crystals were made at the beamline BM02 of European Synchrotron Radiation Facility (ESRF) in Grenoble, France, which is one of the most intense bending magnet beamlines and has an excellent optics producing a small sized parallel incident X-ray flux. The first candidate was a Si crystal with a (111) surface. As is well-known, this crystal has a good energy resolution of some eV. However, the reflection was very small, and it would take one week to obtain one million counts at the $S(Q)$ maximum of Ge–Se glasses. The mosaicking or bending tests of the crystal did not help to improve the count rate drastically.

The second candidate was a graphite crystal having a moderate energy resolution but a high reflection rate. The first trial was made using a usual analyzer attachment with the total arm length of ~ 60 cm, i.e., the length of sample-analyzer and analyzer-detector of 30 cm each. Without a slit in front of the detector, the energy resolution was more than 600 eV FWHM, much worse than a SSD detector. The smallest slit size of 0.5 mm gave ~ 200 eV FWHM, still similar to SSD.

Then, the arm length was extended to reduce the resolution width but to keep the count rate sufficiently high for reasonable beamtimes. Finally, we found that a total arm length of more than 80 cm was the best choice [16]. Figure 3 shows a photograph of our present long detecting system. By optimizing the count rates and resolution width, a resolution of ~ 100 eV FWHM and a count rate of

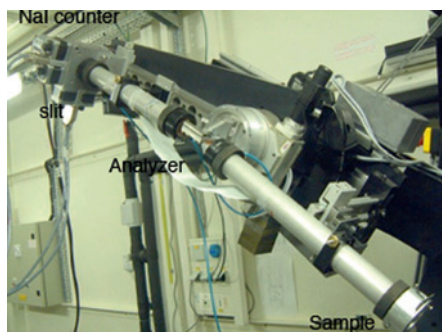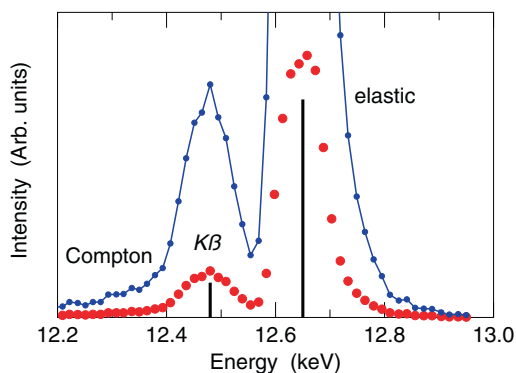**Figure 3:** Photograph of the present detecting system at BM02/ESRF.

Figure 4: Typical energy scan curve using flat graphite crystal analyzer and the detector arm of ~ 80 cm with the energy resolution of ~ 80 eV FWHM. The measurement was performed on $GeSe_2$ glass at the incident energy of 20 eV below the Se K absorption edge at the scattering angle of about 45°. Small circles with line are the same data multiplied by 5. After [12].

~ 1 800 000 counts was obtained near the Se K edge, and ~ 600 000 counts near the Ge K edge during a scan of several hours on the Ge–Se glassy alloys [16]. Note that the previous articles gave better energy resolutions of ~ 90 eV near the Ge K edge, but hereafter, we will refer to the values that are measured near the Se K edge.

Later, the resolution was improved to be 80 eV FWHM while keeping the count rate by optimizing the total arm length of ~ 80 cm [12, 18]. Figure 4 shows a typical energy curve obtained with this detecting system using a flat graphite crystal analyzer on As_2Se_3 glass at the incident X-ray energy 20 eV below the Se K edge measured by simultaneously changing the θ-2θ angles of the analyzer crystal and the detector [12].

The small circles with lines are the same data multiplied by 5 to clarify the Se $K\beta$ fluorescence and Compton scattering intensities. Compared with the data of the a SSD detector shown in Figure 2, the elastic and $K\beta$ fluorescence signals are well separated. These non-elastic contributions can be estimated to be less than 0.2% at the energy of the elastic scattering indicated by the long bar. Nevertheless,
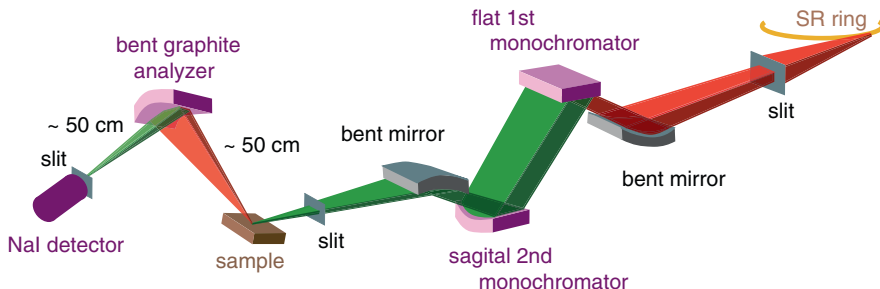
Figure 5: Schematic diagram of the optics at BM02/ESRF and the detecting system using a bent graphite crystal. After [7].

we performed such energy scans to correctly estimate these contributions for the data correction.

Then, we directly derived the $\Delta_k S(Q)$ spectrum by taking the difference between two diffraction data sets around each absorption edge using the procedure given elsewhere [7, 16]. Remaining small Compton scattering contributions near the elastic energies were nearly removed in subtracting the two scattering functions at near- and far-edge incident energies. In fact, this reduced the spurious Compton scattering contribution even at high Q values down to less than 0.005% of the elastic signal.

The next trial was the use of bent graphite crystal for the analyzer [7]. Figure 5 shows the schematic diagram of the optics at BM02/ESRF and the detecting system using a bent graphite crystal. The bent crystal was manufactured by Panasonic C. Ltd. with some different curvatures of the radius 90 mm for low X-ray energies of 9–13 keV (typically Ge, As, and Se K edges), 60 mm for medium energies of 15–25 keV (typically Ag K edge), and 21 mm for high energies of 30–35 keV (typically Sb, Te, and I K edges). The bending was performed in the direction perpendicular to the scattering X-rays, which focuses the vertically scattered X-rays to the detector and allows the energy changes of several keV. Owing to the focusing geometry, the intensities of the scattered X-rays did increase by a factor of 3–4, which allows us to make the detector arm longer to be ∼ 1 m with improving the resolution width of ∼ 70 eV near the Se K edge.

Figure 6 shows a typical energy curve obtained from this detecting system using a bent graphite crystal analyzer on $Ag_{0.15}(GeSe_3)_{0.85}$ glass at the incident X-ray energy 20 eV below the Se K edge measured by simultaneously changing the θ-2θ angles of the analyzer crystal and the detector. The shape of the energy scan is slightly trapezoid-like rather than that using the flat crystal shown in Figure 4. This spectral feature provides a good advantage concerning mis-alignments of the sample position and/or detecting system. Such mis-alignments usually cause
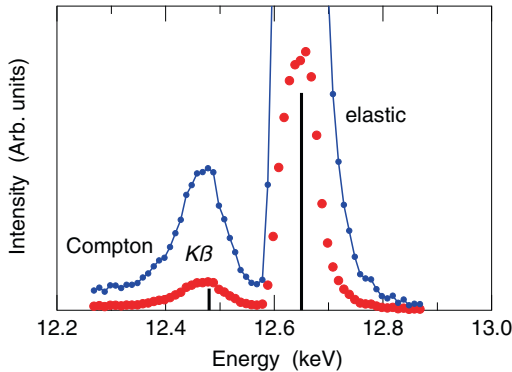
Figure 6: Typical energy scan curve using a bent graphite crystal analyzer and the detector arm of ~ 1 m with the energy resolution of ~ 70 eV FWHM. The measurement was performed on $Ag_{0.15}(GeSe_3)_{0.85}$ glass at the incident energy of 20 eV below the Se K absorption edge at the scattering angle of about $45°$.

a shift of the energy in the detecting system with varying the scattering angle or Q. Namely, remarkable drops of the scattering intensities frequently happen with changing Q when using the flat graphite analyzer exhibiting a comparably sharp peak as a function of the scanned energy. The use of the bent analyzer having a relatively *flat* top in the energy scan spectrum significantly reduced such intensity drops in the intensity data.

Regarding the counting rate, more than four million counts could be collected at the $S(Q)$ maximum, which typically took 3–5 h per scan. Thus, bending the analyzer crystal further improves the statistics in the $\Delta_k S(Q)$ spectrum.

Since the obtained data are mostly elastic signals, the data analysis becomes much easier than that using a SSD detector. The typical duration of the data analysis is about 1 h until obtaining a preliminary $\Delta_k S(Q)$ result, and we can immediately judge if the experiment is successful just after the experiment during a limited beamtime.

It should be emphasized that due to the extremely short blind time a NaI scintillation counter having a blind time of typically ~ 10 ns compared with a SSD detector with about 1 μs, this detecting system can easily be utilized for undulator beamlines to improve the statistic quality further. Such an application was already started by Kohara et al. [32] at BL13XU of the SPring-8, one of the strongest undulator beamlines.

4 Reverse Monte Carlo modeling

Reverse Monte Carlo (RMC) modeling [33–35] is a useful tool to construct three-dimensional (3D) structural models of disordered materials using experimental diffraction data. Many applications of the RMC modeling to network glasses were

reviewed by McGreevy and Zetterström [36]. Typical examples are for vitreous silica SiO_2 by Keen and McGreevy [37], ion conducting glasses by Wicks et al. [38], silicates by Cormier et al. [39], and phosphates by Hoppe et al. [40].

In the RMC simulation technique, atoms of initial configuration are moved so as to minimize the deviation from the data, e.g., $S(Q)$ and $\Delta_k S(Q)$s, by a standard Metropolis Monte Carlo algorithm [41]. A help of neutron diffraction data is also useful to improve the validity of RMC modeling [6, 7, 42–44], in particular, when light elements are included in disordered alloys, for which AXS studies are inapplicable.

A result of a hard-sphere Monte Carlo simulation containing typically 5000–10 000 atoms was used as a starting configuration. Some constraints were applied to the RMC simulation to avoid any physically unreliable structures. Shortest atomic distances were applied for all samples to avoid unreasonable spikes in partial pair distribution functions, $g_{ij}(r)$, in the low r region. Weak bond angle constraints were applied for semiconducting glasses, which were based on other diffraction data. Homopolar wrong bond fractions were also constrained for chalcogenide glasses, for which results of *ab initio* molecular (MD) dynamics simulation were utilized.

RMC simulations were then performed using the RMC++ program package coded by Gereben et al. [35] with differently weighted structure factors and pair distribution functions. A simulating box size was chosen to match the number densities of the samples.

5 Examples

Our new detecting system for AXS measurements was firstly applied to Ge–Se chalcogenide glasses [16, 45–47]. We analyzed the $\Delta_k S(Q)$ data and the corresponding differential pair distribution function, $\Delta_k g(r)$, without the use of RMC modeling. The choice of this glassy system was on the basis of previous investigations, i.e., the local- and intermediate-range structure of $GeSe_2$ glass was the first target of "AXS using SR" by Fuoss et al. [11]. Later, this system was carefully investigated by Petri et al. [28] using neutron diffraction employing isotope substitution (NDIS) technique.

Glassy As_2Se_3 was the second target [48] for the new detecting system, which revealed a remarkable improvement of the statistical quality of the data as compared with our previous AXS measurements on the same sample using a SSD detector [49, 50]. Subsequent to these traditional chalcogenide glasses, some Ag or Cu salts-As_2Se_3 mixtures of room-temperature superionic conducting glasses [51–

53] were measured to confirm the feasibility of the detecting system, and pseudo-binary alloys of salts and As_2Se_3 glass were analyzed from the differential data.

With the help of RMC modeling, at least two important advancements were made in the AXS results.

1. $S_{ij}(Q)$ and $g_{ij}(r)$ functions as well as 3D atomic configurations can be obtained as a typical model for non-crystalline materials, which enabled us to compare with NDIS data [13] and *ab initio* MD simulation results [18] for confirming the reliability of the AXS experiments and RMC model.

2. Since RMC modeling is based on atomic configurations in real space, some corrections can be automatically made in $\Delta_k S(Q)$ data, such as the centering of the oscillations without using Krogh-Moe [54] and Norman [55] corrections and the optimizing of the amplitude of oscillations caused by, e.g., errors in theoretical f' values [17, 18].

These corrections surely helped to make the present AXS technique a highly reliable method for investigating local- and intermediate-range structures of non-crystalline materials.

The most typical results obtained from AXS with RMC modeling is the intermediate-range structures which appears as a prepeak or first sharp diffraction peak (FSDP). It usually appears in $S(Q)$s of chalcogenide glasses, indicating the existence of intermediate-range correlations therein. In the past, the prepeak was considered to reflect the existence of layer structures analogous to the corresponding crystals, or a formation of clusters with a size of $2\pi/Q_p$, where Q_p is the Q position of prepeak. Petri et al. [28] discussed using their NDIS data that the prepeak in $GeSe_2$ glass at $Q \sim 10$ nm^{-1} originates from the Ge–Ge correlation because only $S_{GeGe}(Q)$ has a large prepeak and other partials have no such indications.

RMC modeling on basis of single total scattering experiment on $GeSe_2$ glass, however, gave unreliable $S_{GeGe}(Q)$ results concernig the prepeak [56–58] although the short-range correlations were in good agreement with the NDIS results. For example, Moharram and Abdel-Baset [56] measured X-ray diffraction using a conventional X-ray spectrometer, and the RMC modeling using the $S(Q)$ data indicated the prepeak in $S_{SeSe}(Q)$ partial and the shape of $S_{GeGe}(Q)$ was completely different from the NDIS result. Another RMC modeling with high-energy synchrotron X-ray diffraction by Petkov and Le Messurier [57] could not reproduce a prepeak in $S_{GeGe}(Q)$ and only a shoulder was realized at the prepeak position. Murakami et al. [58] tried a combination of X-ray and neutron diffraction data for the RMC modeling. Although a prepeak could be reproduced in $S_{GeGe}(Q)$, its height was much smaller than that evaluated from the NDIS measurement.

On the other hand, the result of our RMC modeling based on the AXS data [7, 13] revealed a remarkable prepeak in $S_{GeGe}(Q)$, which mostly coincides with the NDIS result. Thus, it can be concluded that the RMC modeling seems to tend to avoid characteristic features of, e.g., a sharp prepeak, and the presence of the element-related information is crucial for reproducing the prepeaks or FSDPs. Therefore, the AXS method is a strong tool to investigate the intermediate-range structure.

In the next subsections, we will review the features of prepeaks or FSDPs in Ge–Se [16, 17] and As–Se [18, 19] chalcogenide glasses, and in $Ge_2Sb_2Te_5$ digital versatile disk (DVD) material [22].

5.1 Ge–Se glasses

Ge–Se glassy alloys are the most typical chalcogenide glasses, and have intensively been investigated as a prototype of covalent glasses. It was believed that the coordination numbers around the Ge and Se atoms (4 and 2, respectively) strictly follows the 8-N bonding rule, where N is the total number of s and p electrons in the outmost electron shells of the atoms. This rule was proposed by Mott [59], who emphasized that according to this rule, all electrons are situated in filled electronic bands so that in contrast to crystalline semiconductors, large changes in the electrical conductivity do not occur in covalent glasses when the composition is only slightly changed [60].

In the past, it was also believed that there are no homopolar bonds called also wrong bonds at the stoichiometric composition of $GeSe_2$. Such a framework of chemically ordered random network model was broken experimentally by Petri et al. [28] using a NDIS technique, where $25 \pm 5\%$ of Ge–Ge and $20 \pm 5\%$ of Se–Se wrong bonds were observed in $GeSe_2$ glass.

Another topic for Ge–Se glasses is the "rigidity percolation theory", the "mean-field constraint theory", or the "stiffness transition theory", which was proposed by Phillips [61] and Thorpe [62]. This theory is a powerful tool for explaining numerous experimentally observed anomalies around the critical composition of the rigidity percolation threshold occurring at an average coordination number $\langle r_C \rangle = 2.40$. There, the number of constraints per atom is equal to the degree of freedom. In the case of Ge_xSe_{1-x} glasses, this corresponds to $x = 0.20$. The character of the network glasses undergoes a steep first-order-like transition from easily deformable (floppy) at $\langle r_C \rangle < 2.40$ to rigid at $\langle r_C \rangle > 2.40$.

Boolchand and coworkers [63, 64] demonstrated that results of Raman scattering, modulated scanning calorimetry, and Mössbauer spectroscopy measured in fine concentration steps provide evidence for a multiplicity of stiffness transi-
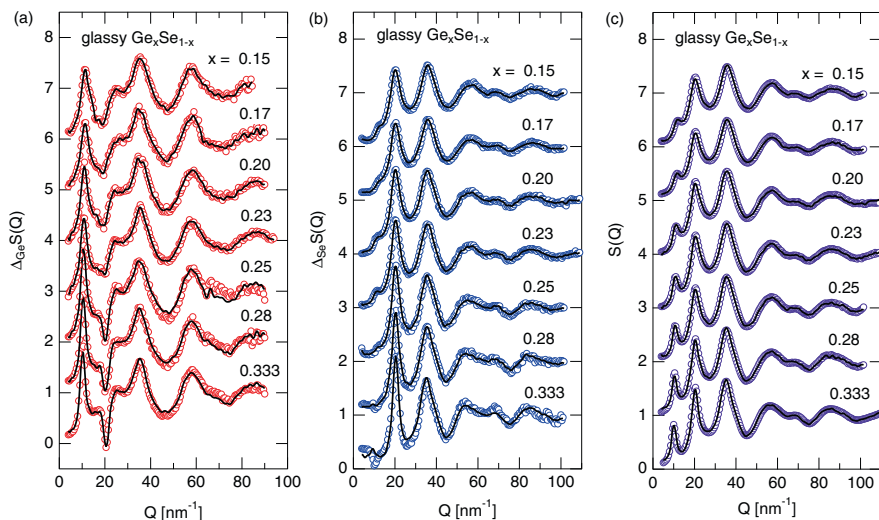
Figure 7: The x dependence of (a) $\Delta_{Ge}S(Q)$, (b) $\Delta_{Se}S(Q)$, and (c) $S(Q)$. Circles: AXS data, Solid curves: RMC results. After [17].

tions with an onset point near $\langle r_C \rangle = 2.40$ ($x = 0.20$) and a completion point near $\langle r_C \rangle = 2.52$ ($x = 0.26$). Of particular interest is the Raman scattering result that showed a shift of the corner-sharing mode frequency for the $Ge(Se_{1/2})_4$ tetrahedral units with varying x. The interpretation of the Raman scattering result should correlate with the intermediate-range atomic structure of glassy Ge_xSe_{1-x} around these stiffness threshold compositions.

The AXS measurements of the Ge_xSe_{1-x} glasses were carried out in a wide concentration range of $x = 0.333–0.15$ [17]. Circles in Figure 7 show the x dependence of (a) $\Delta_{Ge}S(Q)$, (b) $\Delta_{Se}S(Q)$, and (c) $S(Q)$. For all x values, the features of $\Delta_{Ge}S(Q)$ are very different from those of the corresponding $S(Q)$: They have large prepeaks at ~ 10 nm^{-1}. Moreover, there are distinct minima at ~ 20.5 nm^{-1}, where the first peaks are located in total $S(Q)$s. In addition, the second peaks at ~ 35 nm^{-1} have shoulders at ~ 25 nm^{-1}, which locate between the first and second peaks in the $S(Q)$s.

On the other hand, $\Delta_{Se}S(Q)$s show mostly no indications at the prepeak positions in the $S(Q)$s and $\Delta_{Ge}S(Q)$s, and the first peaks are much higher than those in the $S(Q)$s. At higher $Q > 30$ nm^{-1}, the spectral shapes of $\Delta_{Se}S(Q)$s closely resemble those of the corresponding $S(Q)$s. An interesting feature was observed from a detailed inspection of the $\Delta_{Se}S(Q)$ spectra: There are weak shoulders at ~ 15 nm^{-1}. Taking the weighting factors into account, these shoulders can be interpreted as the preference of Se–Se intermediate-range correlations.
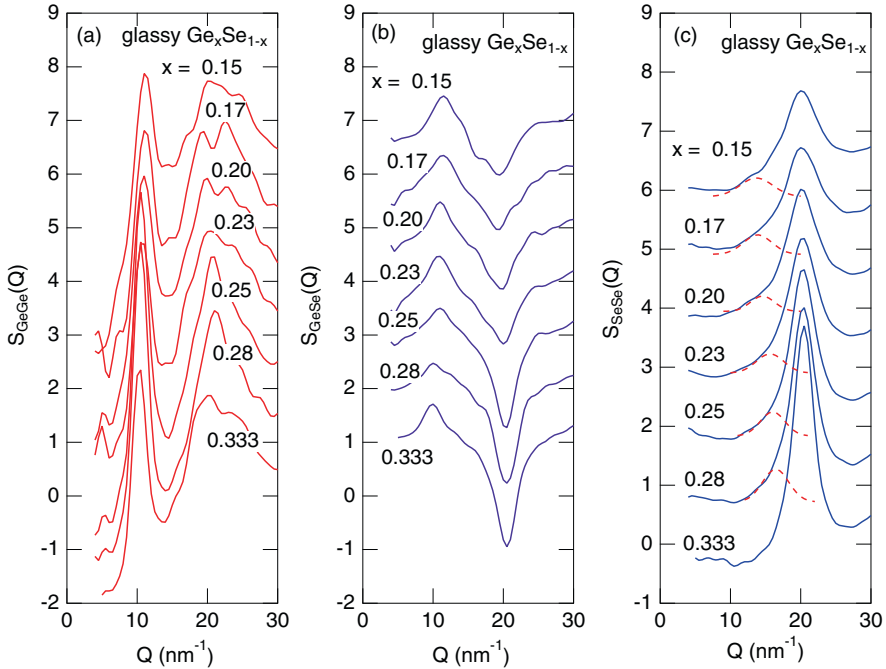
Figure 8: (a) $S_{GeGe}(Q)$, (b) $S_{GeSe}(Q)$, and (c) $S_{SeSe}(Q)$ in the Q region around the pre- and first peak positions in $S(Q)$, obtained from the RMC modeling for Ge_xSe_{1-x} glasses.

    The solid curves in Figure 7 indicate the best fits of the RMC modeling. All of the fit curves coincide well with the corresponding experimental data.

    Figure 8 shows (a) $S_{GeGe}(Q)$, (b) $S_{GeSe}(Q)$, and (c) $S_{SeSe}(Q)$ in the Q region around the pre- and first peak positions in $S(Q)$, obtained from the RMC modeling. At $x = 0.333$, a sharp peak is seen in $S_{GeGe}(Q)$ at $Q \sim 10 \, nm^{-1}$ with a height of ~ 2.5, which is much larger than that in $S(Q)$. The present result is very similar to the NDIS finding by Petri et al. [28], which was discussed elsewhere [13]. The prepeak height decreases with decreasing x. Even at $x = 0.15$, however, it is ~ 2, still higher than the height of the first peak at $\sim 20 \, nm^{-1}$. Moreover, the prepeak position and width do not vary largely with x.

    The prepeak features in $S_{GeGe}(Q)$ are very different from those in $S(Q)$, where with decreasing x, the prepeak rapidly decreases in height and shifts towards higher Q values [65, 66]. Thus, it is concluded that the origin of the prepeak in $S(Q)$ is not limited to the Ge–Ge correlations, but may include other contributions from the Ge–Se and Se–Se correlations as was already assumed earlier [65].

    In the $S_{GeSe}(Q)$ spectrum at $x = 0.333$, there is also a peak observed at the prepeak position of $\sim 10 \, nm^{-1}$. Its Q position remains almost unchanged with de-

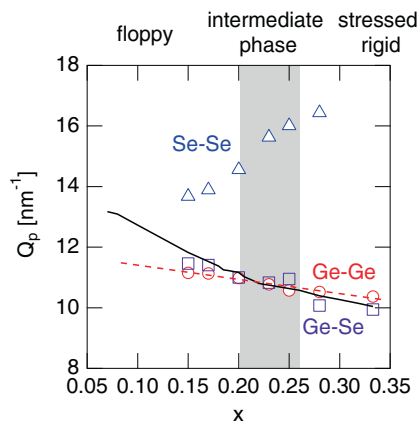**Figure 9:** The x dependence of the prepeak or pre-shoulder positions Q_p observed in $S_{GeGe}(Q)$, $S_{GeSe}(Q)$, and $S_{SeSe}(Q)$, given as circles, squares, and triangles, respectively together with those in $S(Q)$ [65] indicated by the solid curve. The dashed line is a guide for the eyes. After [17].

creasing x. Thus, the contribution of the Ge−Se correlation must be taken into account to understand the origin of the prepeak in $S(Q)$. A steep hump is observed at the first peak position in $S(Q)$, which becomes shallower and broader with decreasing x.

In the $S_{SeSe}(Q)$ spectrum at $x = 0.333$, there is no indication of a peak at the prepeak positions as in the other $S_{ij}(Q)$s. However, a small shoulder at the low Q side of the first peak at ~ 15 nm^{-1} grows up with decreasing x. To exhibit this preshoulder in detail, the spectra were fitted using two pseudo-Voigt functions, i.e., a linear combination of Gaussian and Lorentzian curves, and the obtained preshoulders are shown by the dashed curves in Figure 8. It can be seen that with decreasing x, the pre-shoulder position shifts toward smaller Q values.

Figure 9 shows the x dependence of the prepeak or pre-shoulder positions Q_p observed in $S_{GeGe}(Q)$, $S_{GeSe}(Q)$, and $S_{SeSe}(Q)$, given as circles, squares, and triangles, respectively [17] together with those in $S(Q)$ [65] indicated by the solid curve. The Q_p position in $S_{GeGe}(Q)$ shifts very slightly and linearly toward higher Q values with decreasing x as shown by the dashed line. No anomalies are found in the stiffness transition composition range of Boolchand's criterion, $x = 0.26-0.20$ [63, 64]. A slightly larger shift is observed in the Q_p position in $S_{GeSe}(Q)$, and again it seems to show no effect related to the stiffness transition. On the other hand, a clear decrease is found from ~ 16 to 14 nm^{-1} in $S_{SeSe}(Q)$ with decreasing x, where the largest shift occurs in the intermediate-phase composition range. Thus, the structural change related to the stiffness transition occurs in the Se−Se intermediate-range structure.

5.2 As–Se glasses

As–Se glassy alloys are also the typical chalcogenide glasses. As regards the 8-N bonding rule in relation to the stiffness transition, Boolchand and coworkers [67] only expressed their opposition to the 8-N bonding rule based on the stiffness transition. Their work was carried out using T-modulated differential calorimetry. It was found that non-reserving heat flow almost vanishes in the $0.29 < x < 0.37$ composition range. Since the ideal stiffness transition boundary for the As_xSe_{1-x} glasses should be $x = 0.40$ if the 8-N bonding rule was strictly valid, they proposed a breakdown of this rule and suggested that 28.6% of $Se=As(Se_{1/2})_3$ quasi tetrahedral units should exist in addition to the normal $As(Se_{1/2})_3$ pyramidal units around the As atoms. This idea motivated diffraction and spectroscopic investigations of the local structures in these glasses. However, no experimental evidence could be achieved over the last 15 years owing to experimental difficulties in determining local structures of glassy systems.

On the relation between the prepeaks and the stiffness transition, Bauchy et al. [68] carried out *ab initio* MD simulations on the As_xSe_{1-x} glasses, and found the structural signature for the intermediate phase of Boolchand's criterion in the prepeak or FSDP of the $S_{AsSe}(Q)$ in reciprocal space, and the fraction of the As–As wrong bonds in real space. In their paper, they requested experimentalists to find the partial structural signatures for the intermediate phase in the As_xSe_{1-x} glasses.

The AXS experiments of As_xSe_{1-x} glasses were performed at $x = 0.40$ [18], 0.33, and 0.29 [19], including the above intermediate phase composition. Circles in Figure 10 show the x dependence of (a) $\Delta_{As}S(Q)$, (b) $\Delta_{Se}S(Q)$, and (c) $S(Q)$. For all x values, the features of $\Delta_{As}S(Q)$ are very different from those of the corresponding $S(Q)$: They have distinct and sharp prepeaks at $\sim 12\ nm^{-1}$. Moreover, the first peaks at $\sim 22\ nm^{-1}$ are small compared with those in $S(Q)$s. On the other hand, $\Delta_{Se}S(Q)$s show no indications of the prepeak at $\sim 12\ nm^{-1}$, but have shoulders at $\sim 14.5\ nm^{-1}$.

Solid curves in Figure 10 indicate the best fits of the RMC modeling, which mostly coincide with each of the experimental data.

Figure 11 shows (a) $S_{AsAs}(Q)$, (b) $S_{AsSe}(Q)$, and (c) $S_{SeSe}(Q)$ in the Q region around the pre- and first peak positions in $S(Q)$, obtained from the RMC modeling. At $x = 0.40$, a sharp peak is seen in $S_{AsAs}(Q)$ at $Q \sim 12\ nm^{-1}$ with a height of ~ 0.8, which is much larger than that in $S(Q)$. Thus it is suggested that the As–As correlations dominate the intermediate-range order in this glass. With decreasing x, the prepeak gradually decreases in height and shifts slightly toward lower Q values.
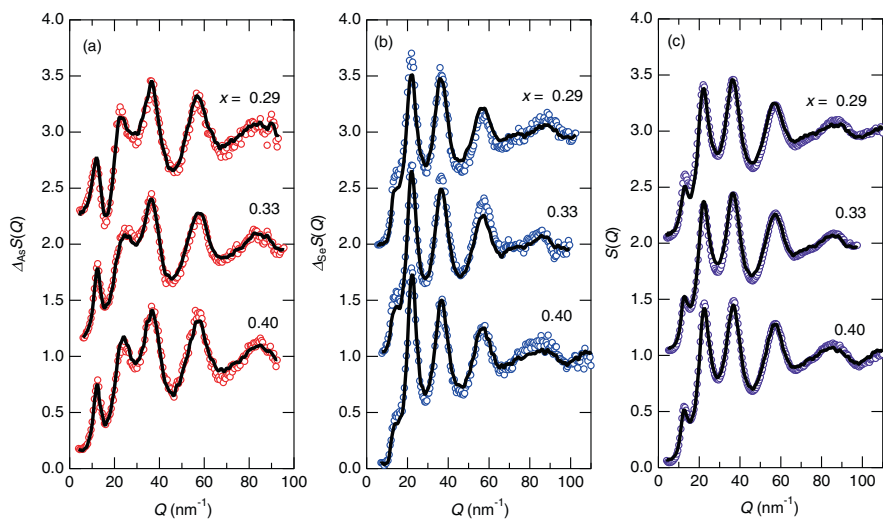
Figure 10: The x dependence of (a) $\Delta_{As}S(Q)$, (b) $\Delta_{Se}S(Q)$, and (c) $S(Q)$. Circles: AXS data, Solid curves: RMC results. After [19].
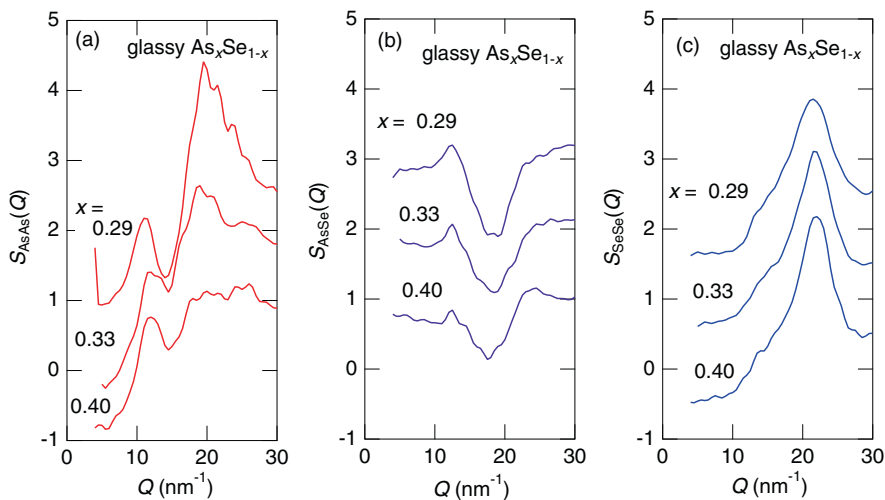

Figure 11: (a) $S_{AsAs}(Q)$, (b) $S_{AsSe}(Q)$, and (c) $S_{SeSe}(Q)$ in the Q region around the pre- and first peak positions in $S(Q)$, obtained from the RMC modeling for As_xSe_{1-x} glasses.
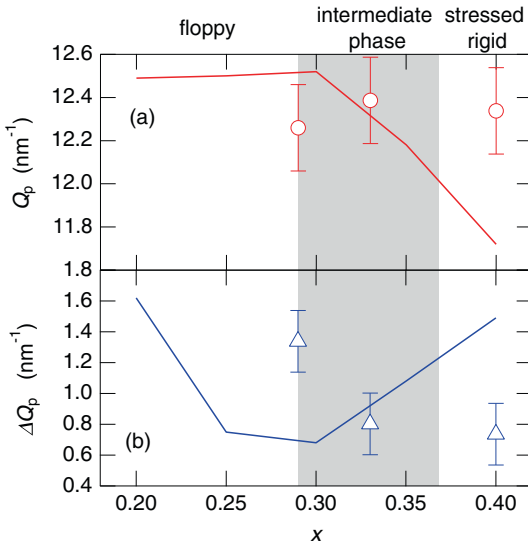
Figure 12: The x dependence of (a) Q_p and (b) ΔQ_p obtained from the AXS measurement (marks) and their *ab initio* MD simulation (lines) for $As_x Se_{1-x}$ glasses. After [19].

In the $S_{AsSe}(Q)$ spectrum at $x = 0.40$, there is also a peak [18] observed near the prepeak position in $S(Q)$ of 12 nm^{-1}. Its Q position remains almost unchanged with decreasing x. Thus, the As–Se contribution should also be taken into account to understand the origin of the prepeak in $S(Q)$ of $As_x Se_{1-x}$ glasses. A steep hump is observed at ~ 18 nm^{-1}, slightly lower than the Q position of the first peak in $S(Q)$, and seems to remain unchanged with decreasing x.

In the $S_{SeSe}(Q)$ spectrum at $x = 0.40$, there is no indication of a peak at the prepeak positions as in the other $S_{ij}(Q)$s. However, there is a small shoulder at the low Q side of the first peak of ~ 14.5 nm^{-1}, which gradually grows up with decreasing x. The first peak at $x = 0.40$ has a height of ~ 2.2, which rapidly decreases with decreasing x.

Concerning the relation of $S_{ij}(Q)$s to the stiffness transition, Bauchy et al. [68] concluded from the *ab initio* MD simulation that at $x \sim 0.30$, the characteristic parameters of the prepeak in $S_{AsSe}(Q)$ shows a threshold for the prepeak position, Q_p, and a minimum for the prepeak width, ΔQ_p. Figure 12 shows the x dependence of (a) Q_p and (b) ΔQ_p obtained from the AXS measurement (marks) and their *ab initio* MD simulation (lines). The figure is taken from [19].

At a glance, the AXS values are not in agreement with the *ab initio* MD results, in the x dependence of both the experimental prepeak position and width, i.e., the position of the $S_{AsSe}(Q)$ functions mostly keeps the same values of ~ 12.3 nm^{-1} in the whole concentration range measured and the width becomes even broadened at $x \sim 0.29$, which are completely different features from the theoretical ones. For

further discussion, AXS measurements in the lower x region of the floppy glasses should be performed, which are now in progress.

5.3 Amorphous Ge$_2$Sb$_2$Te$_5$

Rewritable optical storage devices like DVD or blu-ray have meanwhile become common media for data storage and are used in all areas of daily life. The writing/erasing process on these devices is attained by a reversible laser-induced crystalline-amorphous transition of the so-called phase change materials, such as Ge$_2$Sb$_2$Te$_5$ (GST). The transition occurs on a time scale of a several ten ns [69], and is accompanied by a significant change of the optical and electrical properties. On the other hand, both the phases should be sufficiently stable for more than ten years at ambient conditions. The important step toward an understanding of the phase change mechanism is a detailed knowledge of the atomic structure participating in the phase transition.

The structure of crystalline GST film is relatively well understood by a powder XRD experiment [70]; it does not exhibit the stable hexagonal crystal structure in ambient conditions, but a metastable rocksalt structure, with Te atoms occupying sites on one *fcc* sublattice and with Ge, Sb, and 20% of vacancies forming another *fcc* sublattice. Convincing evidence for pronounced lattice distortions was found in an XAFS experiment by Kolobov et al. [71]; six Ge–Te neighboring bonds of the octahedral symmetry sites of the rocksalt structure separate into three shorter and three longer bonds, as in GeTe crystal [72].

The amorphous phase was also explored with XAFS by Kolobov et al. [71], who found remarkable decreases of Ge–Te and Sb–Te covalent bond lengths from those in the crystal. The XAFS data also indicated a change in the coordination number around Ge from six in the crystal to four in the amorphous phase. Kohara et al. [73] measured total $S(Q)$ of the amorphous phase using high-energy XRD and analyzed the data using RMC calculation. By combining X-ray and neutron diffraction with XAFS, Jóvári et al. [74] performed a RMC analysis. Although the reliability of the RMC output may be improved, XAFS data do not help for investigating intermediate-range structures of amorphous GST.

To investigate the local- and intermediate-range order in amorphous GST, AXS experiments were carried out at energies close to the Ge, Sb, and Te K edges [22]. Figure 13(a) shows $\Delta_k S(Q)$s obtained from AXS measurements close to the Ge (red circles), Sb (purple circles), and Te (blue circles) K edges, together with $S(Q)$ given by black circles. Solid curves in the figure show the best fits of the RMC modeling, which coincide well with the experimental data.
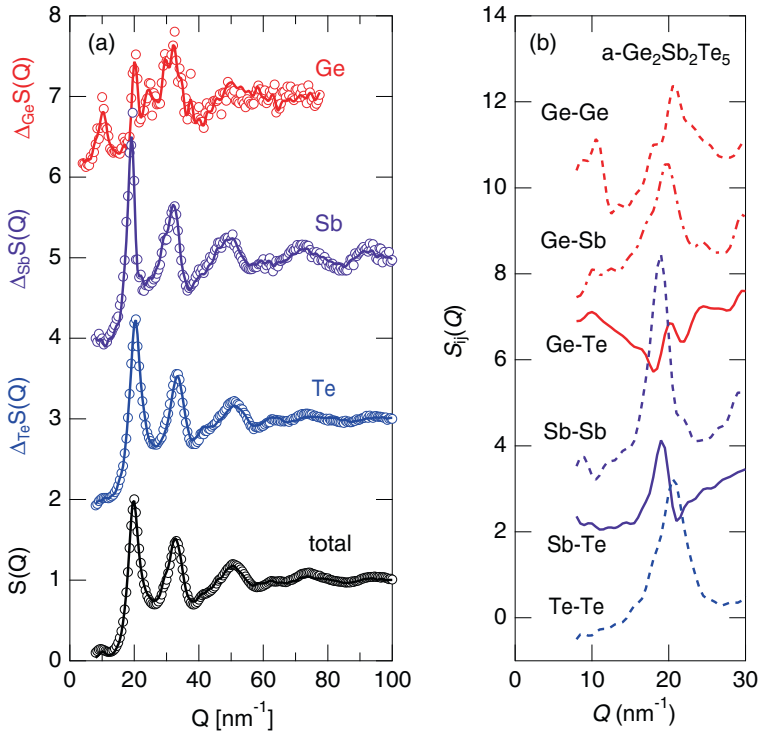
Figure 13: (a) $\Delta_k S(Q)$s of amorphous $Ge_2Sb_2Te_5$ film obtained from AXS measurements (circles) and RMC fits (curves), and (b) $S_{ij}(Q)$s in the Q region around the pre- and first peak positions in $S(Q)$. After [22].

These functions already indicate some interesting features. A small prepeak is observed in $S(Q)$ at $\sim 10\ nm^{-1}$, indicating the existence of an intermediate-range atomic correlation. At this Q position, $\Delta_{Ge}S(Q)$ has a prominent peak, while $\Delta_{Sb}S(Q)$ and $\Delta_{Te}S(Q)$ show only small peaks similar in $S(Q)$. Also, $\Delta_{Ge}S(Q)$ provides only a small contribution to the distinct first maximum in $S(Q)$ at $\sim 20\ nm^{-1}$. On the other hand, this feature is hardly seen in $\Delta_{Sb}S(Q)$ and $\Delta_{Te}S(Q)$, which are very similar to $S(Q)$. Thus, there is no doubt that the atomic arrangements around the Ge atoms are considerably different from the sites of the other constituents in the amorphous phase.

Figure 13(b) shows $S_{ij}(Q)$s in the Q region around the pre- and first peak positions in $S(Q)$, obtained from the RMC modeling for the AXS data. The features of Sb–Te related partials are basically similar to each other with slight differences in the positions and heights of the first peaks, indicating similar local environments around the Sb and Te atoms, as in the metastable rocksalt crystal. On the other

hand, the Ge–Te related partials, $S_{GeGe}(Q)$, $S_{GeTe}(Q)$, and $S_{TeTe}(Q)$ show their own characteristic features.

It is interesting that these Ge–Te related partials resemble well those of GeSe$_2$ glass shown in Figure 8, i.e., 1) the Ge–Ge correlation shows a prominent prepeak indicating the existence of intermediate-range order, and 2) the Ge-chalcogen partial structure has a minimum at the first peak position in $S(Q)$. GeSe$_2$ is a typical chalcogenide glass, in which the coordination number around Ge follows the 8-N bonding rule of four. Thus the amorphous structure of GST around the Ge atoms is expected to be very different from the three- or six-fold coordinated crystal.

Ohara et al. [75] performed another AXS experiment on GST close to the Sb and Te K edges at BL02B1/SPring-8 using a traditional Ge SSD detector. Compared with their differential data, the statistical quality of our data shown in Figure 12(a) is excellent, probably due to our new detecting system. For the further discussion on the intermediate-range order in GST, comparison of the $S_{ij}(Q)$ data is necessary, which are, however, not displayed in their article. Moreover, papers of *ab initio* MD simulations by Akola and Jones [76, 77], Hegedüs and Elliott [78], or Micoulaut et al. [79], as well as of diffraction and XAFS experiments by Jóvári et al. [74] only discussed the local- and intermediate-range structures in real space. At present, thus, there is no way to examine the validity of the characteristic features of the prepeak in the Ge–Ge correlations.

6 Concluding remarks and perspective

We have developed a new detecting system, which could fully utilize intense X-ray fluxes from third-generation SR facilities, and solved several difficult issues for the structural characterizations of non-crystalline multi-component materials, such as good energy resolution, sufficient count rates during a limited beamtime of the SR facilities, and time-consuming data analysis. Using this detecting system, we have carried out many AXS experiments at the beamline BM02 of the ESRF on several semiconducting glasses. The obtained differential structure factors were analyzed using reverse Monte Carlo modeling to draw three-dimensional atomic configurations.

In this article, we review results of semiconducting glasses, and describe the structure-property relations in these glasses. In particular, the origin of the prepeaks or FSDPs, appearing as a benchmark of intermediate-range order in most of the chalcogenide glasses, could be experimentally examined in detail. The actual origin of the prepeaks can be discussed by the features of $S_{ij}(Q)$s obtained from the AXS + RMC works.

We hope that the AXS experiments in combination with RMC modeling is capable to become a standard method for investigating local- and intermediate-range atomic structures in multi-component non-crystalline materials. Moreover, time-resolved AXS measurements for e.g., phase change materials can be realized in the near future using more intense flux from undulator insertion device and a faster X-ray detector.

References

1. H. M. Rietveld, J. Appl. Cryst. **2** (1969) 65.
2. Y. Waseda, *The Structure of Non-Crystalline Materials*, McGraw-Hill, New York (1980).
3. Y. Waseda, *Novel Application of Anomalous (Resonance) X-ray Scattering for Structural Characterization of Disordered Materials*, Springer-Verlag, Heidelberg (1984).
4. Y. Waseda, *Anomalous X-ray Scattering for Materials Characterization*, Springer-Verlag, Heidelberg (2002).
5. G. H. Bezerra, L. Q. Amaral, A. F. Craievich, and D. Raoux, J. Non-Cryst. Solids **126** (1990) 239.
6. H. E. Fischer, A. C. Barnes, and P. S. Salmon, Rep. Prog. Phys. **69** (2006) 233.
7. S. Hosokawa, W.-C. Pilgrim, J.-F. Bérar, and S. Kohara, Eur. Phys. J.-Spec. Top. **208** (2012) 291.
8. P. Bondot, Acta Cryst. A **30** (1974) 470.
9. Y. Waseda and S. Tamaki, Philos. Mag. **32** (1975) 951.
10. Y. Waseda and S. Tamaki, Z. Phys. B **23** (1976) 315.
11. P. H. Fuoss, P. Eisenberger, W. K. Warburton, and A. Bienenstock, Phys. Rev. Lett. **46** (1981) 1537.
12. S. Hosokawa and J.-F. Bérar, AIP Conf. Proc. **879** (2007) 1743.
13. S. Hosokawa, W.-C. Pilgrim, J.-F. Bérar, and S. Kohara, Phys. Status Solidi A **208** (2011) 2544.

14. S. Hosokawa, Mater. Sci. Forum **783–786** (2014) 1907.
15. S. Hosokawa, J. Stellhorn, and W.-C. Pilgrim, MRS Proceedings **1757** (2015) mrsf14-1757-uu06-05.
16. S. Hosokawa, Y. Wang, J.-F. Bérar, J. Greif, W.-C. Pilgrim, and K. Murase, Z. Phys. Chem. **206** (2002) 1219.
17. S. Hosokawa, I. Oh, M. Sakurai, W.-C. Pilgrim, N. Boudet, and J.-F. Bérar, Phys. Rev. B **84** (2011) 014201.
18. S. Hosokawa, A. Koura, J.-F. Bérar, W.-C. Pilgrim, S. Kohara, and F. Shimojo, Europhys. Lett. **102** (2013) 66008-1-6.
19. S. Hosokawa, W.-C. Pilgrim, J.-F. Bérar, and P. Boolchand, J. Non-Cryst. Solids, DOI 10.1016/j.jnoncrysol.2015.04.018.
20. J. Stellhorn, S. Hosokawa, Y. Kawakita, D. Gies, W.-C. Pilgrim, K. Hayashi, K. Ohoyama, N. Blanc, and N. Boudet, J. Non-Cryst. Solids, DOI 10.1016/j.jnoncrysol.2015.02.027.
21. J. Stellhorn, S. Hosokawa, Y. Kawakita, D. Gies, W.-C. Pilgrim, K. Hayashi, K. Ohoyama, N. Blanc, and N. Boudet, Z. Phys. Chem., DOI 10.1515/zpch-2015-0667.
22. S. Hosokawa, W.-C. Pilgrim, A. Höhle, D. Szubrin, N. Boudet, J.-F. Bérar, and K. Maruyama, J. Appl. Phys. **111** (2012) 083517.
23. J. R. Stellhorn, S. Hosokawa, and W.-C. Pilgrim, Z. Phys. Chem. **228** (2014) 1005.
24. R. W. James, *The Optical Principles of the Diffraction of X Rays*, G. Bell and Sons, London (1962).
25. D. T. Cromer and D. Liberman, J. Chem. Phys. **53** (1970) 1891.
26. S. Sasaki, *Numerical Tables of Anomalous Scattering Factors Calculated by the Cromer and Liberman's Method*, Nat. Lab. High Energy Phys., Tsukuba (1989), p. 1.
27. M. Yoshizawa, S.-M. Zhou, R. Negishi, T. Fukamachia, and T. Kawamura, Acta Cryst. A **61** (2005) 553.
28. I. Petri, P. S. Salmon, and H. E. Fischer, Phys. Rev. Lett. **84** (2000) 2413.
29. Y. Waseda and M. Saito, J. Jpn. Soc. Syn. Rad. Res. **10** (1997) 299.
30. S. Hosokawa, Y. Kawakita, W.-C. Pilgrim, and F. Hensel, J. Non-Cryst. Solids **293–295** (2001) 153.
31. H. Oyanagi, M. Martini, and M. Saito, Nucl. Instrum. Meth. A **403** (1998) 58.
32. S. Kohara, H. Tajiri, C. H. Song, K. Ohara, L. Temleitner, K. Sugimito, A. Fujiwara, L. Pusztai, T. Usuki, S. Hosokawa, Y. Benino, N. Kitamura, and K. Fukumi, J. Phys. Conf. Ser. **502** (2014) 012014.
33. R. L. McGreevy and L. Pusztai, Mol. Simulat. **1** (1988) 359.
34. R. L. McGreevy and M. A. Howe, Annu. Rev. Mater. Sci. **22** (1992) 217.
35. O. Gereben, P. Jóvári, L. Temleitner, and L. Pusztai, J. Optoelectron. Adv. M. **9** (2007) 3021.
36. R. L. McGreevy and P. Zetterström, J. Non-Cryst. Solids **293–295** (2001) 297.
37. D. A. Keen and R. L. McGreevy, Nature **344** (1990) 423.
38. J. D. Wicks, L. Börjesson, G. Bushnell-Wye, W. S. Howells, and R. L. McGreevy, Phys. Rev. Lett. **74** (1995) 726.
39. L. Cormier, G. Calas, S. Creux, and P. H. Gaskell, Phys. Rev. B **59** (1999) 13517.
40. U. Hoppe, R. Kranold, D. Stachel, A. Barz, and A. C. Hannon, J. Non-Cryst. Solids **232–234** (1998) 44.
41. N. Metropolis, A. W. Rosenbluth, M. N. Rosenbluth, A. H. Teller, and E. Teller, J. Phys. Chem. **21** (1953) 1087.
42. A. C. Barnes, S. B. Lague, M. A. Hamilton, H. E. Fischer, A. N. Fitch, and E. Dooryhee, J. Phys.-Condens. Mat. **10** (1998) L645.

43. S. Hosokawa, J.-F. Bérar, N. Boudet, S. Kohara, J. Stellhorn, W.-C. Pilgrim, A. Zeidler, H. Kato, Y. Kawakita, and T. Otomo, J. Phys.-Conf. Ser. **502** (2014) 012023.
44. S. Hosokawa, J. Stellhorn, W.-C. Pilgrim, N. Boudet, N. Blanc, S. Kohara, H. Tajiri, H. Kato, Y. Kawakita, and T. Otomo, Jpn. Phys. Soc. Conf. Proc. **8** (2015) 031002.
45. S. Hosokawa, W.-C. Pilgrim, Y. Kawakita, Y. Wang, J.-F. Bérar, and K. Murase, Phys. Chem. Glasses **43C** (2002) 175.
46. S. Hosokawa, Y. Wang, M. Sakurai, J.-F. Bérar, W.-C. Pilgrim, and K. Murase, J. Non-Cryst. Solids **326–327** (2003) 394.
47. S. Hosokawa, Y. Wang, J.-F. Bérar, M. Sakurai, and W.-C. Pilgrim, and K. Murase, Nucl. Instrum. Meth. B **199** (2003) 165.
48. S. Hosokawa, Y. Wang, W.-C. Pilgrim, J.-F. Bérar, S. Mamedov, and P. Boolchand, J. Non-Cryst. Solids **352** (2006) 1517.
49. S. Hosokawa, A. Goldbach, M. Boll, and F. Hensel, Phys. Status Solidi B **215** (1999) 785.
50. S. Hosokawa, Y. Kawakita, W.-C. Pilgrim, and F. Hensel, J. Non-Cryst. Solids **293–295** (2001) 153.
51. T. Usuki, S. Hosokawa, and J.-F. Bérar, Nucl. Instrum. Meth. B **238** (2005) 124.
52. T. Usuki, S. Hosokawa, and J.-F. Bérar, J. Non-Cryst. Solids **352** (2006) 1514.
53. S. Hosokawa, T. Usuki, N. Boudet, and J.-F. Bérar, Solid State Ionics **180** (2009) 517.
54. Krogh-J. Moe, Acta Cryst. **9** (1956) 951.
55. N. Norman, Acta Cryst. **10** (1957) 370.
56. A. H. Moharram and A. M. Abdel-Baset, Physica B **405** (2010) 4240.
57. V. Petkov and D. Le Messurier, J. Phys.-Condens. Mat. **22** (2010) 115402.
58. Y. Murakami, T. Usuki, M. Sakurai, and S. Kohara, Mat. Sci. Eng. A-Struct. **449–451** (2007) 544.
59. N. F. Mott, Philos. Mag. **19** (1969) 835.
60. N. F. Mott and E. A. Davis, *Electronic Processes in Non-Crystalline Materials*, Oxford University Press, Oxford (1971).
61. J. C. Phillips, J. Non-Cryst. Solids **34** (1979) 153.
62. M. F. Thorpe, J. Non-Cryst. Solids **57** (1983) 355.
63. X. Feng, W. J. Bresser, and P. Boolchand, Phys. Rev. Lett. **78** (1977) 4422.
64. P. Boolchand, X. Feng, and W. J. Bresser, J. Non-Cryst. Solids **293–295** (2001) 348.
65. Y. Wang, E. Ohata, S. Hosokawa, M. Sakurai, and E. Matsubara, J. Non-Cryst. Solids **337** (2004) 54.
66. M. T. M. Shatnawi, C. L. Farrow, P. Chen, P. Boolchand, A. Sartbaeva, M. F. Thorpe, and S. J. L. Billinge, Phys. Rev. B **77** (2008) 094134.
67. D. G. Georgiev, P. Boolchand, and M. Micoulaut, Phys. Rev. B **62** (2000) R9228.
68. M. Bauchy, M. Micoulaut, M. Boero, and C. Massobrio, Phys. Rev. Lett. **110** (2013) 165501.
69. N. Yamada, E. Ohno, K. Nishiuchi, N. Akahira, and M. Takao, J. Appl. Phys. **69** (1991) 2849.
70. N. Yamada and T. Matsunaga, J. Appl. Phys. **88** (2000) 7020.
71. A. V. Kolobov, P. Fons, A. I. Frenkel, A. L. Ankudinov, J. Tominaga, and T. Uruga, Nat. Mater. **3** (2004) 703.
72. T. Chattopadhyay, J. X. Boucherle, and von H. G. Schnering, j. Phys. C Solid State **20** (1987) 1431.
73. S. Kohara, K. Kato, S. Kimura, H. Tanaka, T. Usuki, K. Suzuya, H. Tanaka, Y. Moritomo, T. Matsunaga, N. Yamada, Y. Tanaka, H. Suematsu, and M. Takata, Appl. Phys. Lett. **89** (2006) 201910.

74. P. Jóvári, I. Kaban, J. Steiner, B. Beuneu, A. Schöps, and A. Webb, J. Phys.-Condens. Mat. **19** (2007) 335212.
75. K. Ohara, L. Temleitner, K. Sugimoto, S. Kohara, T. Matsunaga, L. Pusztai, M. Itou, H. Ohsumi, R. Kojima, N. Yamada, T. Usuki, A. Fujiwara, and M. Takata, Adv. Funct. Mater. **22** (2012) 2251.
76. J. Akola, R. O. Jones, S. Kohara, S. Kimura, K. Kobayashi, M. Takata, T. Matsunaga, R. Kojima, and N. Yamada, Phys. Rev. B **80** (2009) 020201(R).
77. J. Akola and R. O. Jones, Phys. Status Solidi B **249** (2012) 1851.
78. J. Hegedüs and S. R. Elliott, Nat. Mater. **7** (2008) 399.
79. M. Micoulaut, J.-Y. Raty, C. Otjacques, and C. Bichara, Phys. Rev. B **81** (2010) 174206.